Heat flux reconstruction and effective diffusion estimation from perturbative experiments using advanced filtering and confidence analysis

M. van Berkel[1,2]**, T. Kobayashi**[3]**, G. Vandersteen**[2]**,
H.J. Zwart**[4,5]**, H. Igami**[3]**, S. Kubo**[3]**, N. Tamura**[3]**,
H. Tsuchiya**[3]**, M.R. de Baar**[1,6]**, and the LHD Experiment
Group**

[1]DIFFER-Dutch Institute for Fundamental Energy Research, PO Box 6336,
5600 HH Eindhoven, The Netherlands
[2]Vrije Universiteit Brussel (VUB), Dept. of Fundamental Electricity and
Instrumentation, Pleinlaan 2, 1050 Brussels, Belgium[4]
[3]National Institute for Fusion Science, 322-6 Oroshi-cho, Toki-city, Gifu,
509-5292, Japan
[4]Eindhoven University of Technology, Dept. of Mechanical Engineering,
Dynamics and Control Group, PO Box 513, 5600MB Eindhoven, The
Netherlands
[5]University of Twente, Dept. of Applied Mathematics, PO Box 217, 7500AE,
Enschede, The Netherlands
[6]Eindhoven University of Technology, Dept. of Mechanical Engineering, Control
Systems Technology group, PO Box 513, 5600 MB Eindhoven, The Netherlands

Abstract. The heat flux is one of the key theoretical concepts used to quantify
and understand transport in fusion devices. In this paper, a new method is
introduced to calculate the heat flux including its confidence with high accuracy
based on perturbed measurements such as the electron temperature. The new
method is based on ideal filtering to optimally reduce the noise contributions
on the measurements and piece-wise polynomial approximations to calculate the
time derivative. Both methods are necessary to arrive at a heat flux and effective
diffusion coefficient with high accuracy. The new methodology is applied to
a measurement example using electron cyclotron resonance heating block-wave
modulation at the Large Helical Device showing the merit of the newly developed
methodology.

1. Introduction

The heat flux is one of the key theoretical concepts used to quantify and understand transport in fusion devices. However, the heat flux q cannot be directly measured and consequently needs to be estimated in some way. Generally, a specific structure for the heat flux is defined, e.g., in terms of a diffusion coefficient χ and convective velocity V (pinch term). These terms χ and V are then estimated from the experimental data and can then be used to reconstruct the heat flux [1, 2, 3, 4]. However, predefining the structure of the heat flux imposes which physical mechanisms determine the heat flux. Consequently, new or different physics that may also contribute to the heat flux cannot be identified and assessed choosing such an approach. Even worse, imposing the wrong structure can lead to erroneous estimates of the transport coefficients and will lead to apparent frequency dependency of transport coefficients or false non-linear dependencies of transport coefficients on for instance the gradients ∇T or T. Hence, an alternative approach is to estimate the heat flux directly from its definition in the heat equation. This was first introduced in [5] and is closely related to the power balance analysis. In [6], this was used to asses the perturbation only and used on measurement data. This became possible due to the improved signal-to-noise ratio's of the electron-cyclotron-emission measurements.

In this paper, we significantly optimize the approach in [6] using advanced filtering methodologies, which allows for the direct calculation of the diffusion coefficient and other physical parameters. The heat flux is evaluated in non steady-state such that the different components of heat transport can be distinguished. Given the complexity of the filtering methodologies applied, the physics discussions for various measurements will be performed in a complementary paper. This paper will focus on the calculation procedure, filtering techniques, and statistical analysis and presents an alternative approach for estimating the diffusion coefficient compared to standard strategies which impose a heat-flux structure [7, 8]. Measurements will be used from the Large Helical Device (LHD). Although this paper does not address directly physics, the reconstruction is essentially based on the physics and clearly shows that the heat pinch (V) has no relevance in the Large Helical Device.

The paper is structured as follows. Sec. 2 discusses the calculation of the heat flux and various heat flux models from the literature. Sec. 3 discusses the variance calculation of the temperature measurements and the ideal filtering technique. Then, Sec. 4 discusses the derivative calculation, one of the key issues in the heat flux calculation. It introduces two methodologies to calculate the temperature derivatives. Sec. 5 describes how to reconstruct heat flux and how to estimate the effective diffusion coefficient. Finally, some conclusions are summarized.

2. Thermal transport and inversion

This section discusses various heat flux models, how they would appear in the standard transport paradigm of the electron heat flux q_e plotted against the product of density and spatial derivative of the electron temperature $-n_e\nabla_\rho T_e$, and how the heat flux can be calculated. Although this methodology is applicable in different transport channels, in this paper we focus on the electron heat transport.

2.1. Heat equation

Electron heat transport in fusion devices is generally described by the heat equation in one-dimension

$$\frac{\partial}{\partial t}\left(n_e T_e\left(\rho,t\right)\right) = \nabla_\rho\left(-q_e\left(\rho,t\right)\right) + p\left(\rho,t\right), \quad (1)$$

where $T_e\left(\rho,t\right)$ is the electron temperature, ρ the normalized radius, n_e the electron density, and $p\left(\rho,t\right)$ the heating power density.

2.2. Heat flux models

Generally, the heat flux is calculated based on a predefined structure. The standard structure used in the fusion literature is based on Fourier's law [4]

$$q_e = -n_e\chi_e\nabla_\rho T_e, \quad (2)$$

where χ_e is the diffusion coefficient. If the heat flux q_e is plotted against $-n_e\nabla_\rho T_e$, the diffusion coefficient is the slope of the line. This is also shown in Fig. 1, which has been calculated using the method introduced in this paper. The underlying temperature used to calculate the heat flux in Fig. 1 is based on (1) and (2).
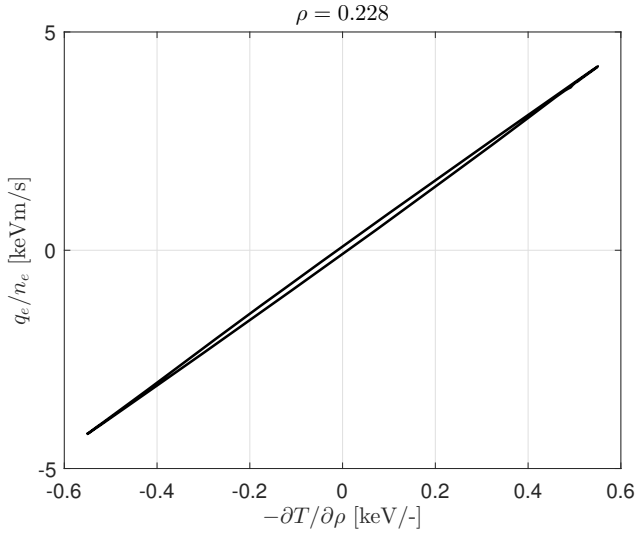
Figure 1. Reconstruction of the heat flux based on a finite difference simulation of (1). The slight opening of the two-lines is due to numerical errors in the finite difference approximation. Moreover, only the heat flux due to a change in perturbation is shown (otherwise it would be always positive).

Heat flux models [reference]		Type
$q_e = -n_e \chi_e \nabla_\rho T_e$	[4]	linear
$q_e = -n_e \chi_e \left(\nabla_\rho T \right) \nabla_\rho T_e$	[9]	non-linear
$q_e = -n_e \chi_e \nabla_\rho T_e - n_e V_e T_e$	[10]	linear
$q_e = -n_e \chi_e \left(P \right) \nabla_\rho T_e$	[5]	non-linear
$q_e = q_0 \left(P \right) - n_e \chi_e \nabla_\rho T_e$	[11]	(non-)linear

Table 1. Common heat flux models in the literature, where P is a proxy for a heat flux dependency on the time scale of $p \left(\rho, t \right)$.

A number of alternative transport models based on experimental observations are proposed in the literature. Generally, these models are based on how the diffusion coefficient changes with respect to various other plasma parameters or follow from the linearization of non-linear or coupled transport equations. A number of these standard and less standard transport models are presented in Table. 1, which are interesting to study in the $q_e - \nabla_\rho T_e$ plane. A graphical depiction of how a number of these dependencies would look like in the $q_e - \nabla_\rho T_e$-plane is shown in Fig. 2. Important to note is that the q_e dependencies explicitly depends on $p \left(\rho, t \right)$ are only valid for a block-wave modulation waveform. Moreover, combinations of these dependencies are also possible.

2.3. Direct calculation of the heat flux

The mathematical calculation of the heat flux is straightforward and is based on rewriting (1) in terms

of q_e, which in cylindrical form is given by

$$\frac{\partial}{\partial t} \left(n_e T_e \left(\rho, t \right) \right) = \frac{1}{\rho} \frac{\partial}{\partial \rho} \left(-\rho \, q_e \left(\rho, t \right) \right) + p \left(\rho, t \right), \quad (3)$$

such that

$$q_e \left(\rho, t \right) = \frac{1}{\rho} \int_0^\rho \rho \left(\frac{\partial}{\partial t} \left(n_e T_e \left(\rho, t \right) \right) - p \left(\rho, t \right) \right) d\rho. \quad (4)$$

In principle, also other terms can appear such as terms related to the linearization of coupled transport coefficients. An example is the ion-electron equilibration, which appears as a damping term τ_{inv} [8]. These terms can either be taken into account explicitly, i.e.,

$$q_e \left(\rho, t \right) = \frac{1}{\rho} \int_0^\rho \rho \left(\frac{\partial}{\partial t} \left(n_e T_e \left(\rho, t \right) \right) - p \left(\rho, t \right) \right.$$
$$\left. - \rho \tau_{inv} \left(\rho \right) T_e \left(\rho, t \right) \right) d\rho, \quad (5)$$

or can be treated as contribution to the heat flux. Moreover, the heating term can consist of a number of other power contributions such as neutral beam injection $p_{nbi} \left(\rho \right)$, ion cyclotron heating $p_{ich} \left(\rho \right)$, and electron cyclotron heating $p_{ech} \left(\rho, t \right)$. It is not always clear what the exact deposition profiles are, hence, calculating the perturbative heat flux based on only the heating terms that are perturbed is a more reliable option than calculating the full heat flux. This still allows to distinguish between the different heat flux dependencies on other plasma parameters around an operating point, but the absolute values of the heat flux have less meaning.

In the next section, the temperature signals are filtered such that the derivatives necessary to determine the (perturbative) heat flux can be calculated.

3. Filtering of temperature

This section introduces the ideal filtering technique and a stochastic confidence analysis to arrive at temperature profiles with a significant improvement in signal-to-noise ratio (SNR) without modifying the relevant signal information. This allows for a proper estimate of the time derivative of the temperature necessary to estimate the time dependent heat flux in (4). For completeness also the experimental conditions of the discharge analyzed are briefly discussed.

3.1. Experimental set-up and conditions

As in this paper the same time trace as in [6] is used to show the optimized methodology, briefly the

September 21, 2018
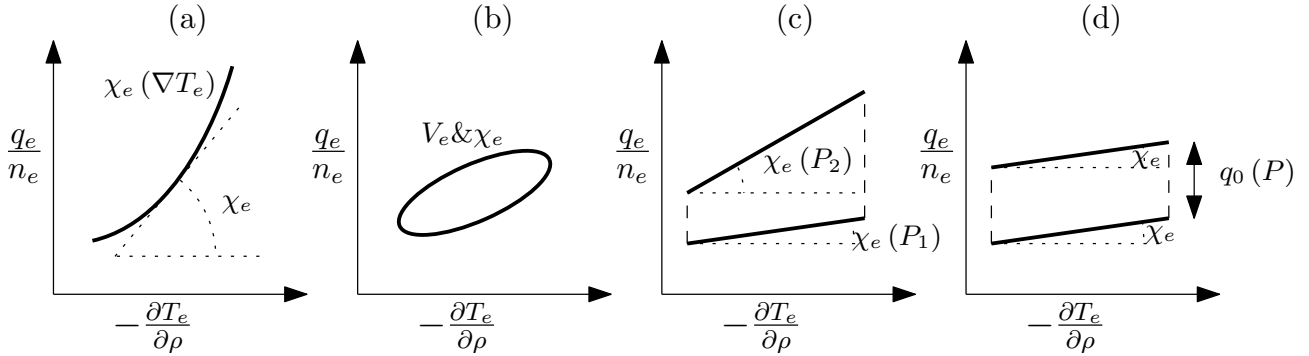
Figure 2. Projection of the heat flux against the spatial temperature gradient as a result of various heat flux dependencies on plasma parameters, (a) $q_e = -n_e \chi_e (\nabla_\rho T) \nabla_\rho T_e$, (b) $q_e = -n_e \chi_e \nabla_\rho T_e - n_e V_e T_e$, (c) $q_e = -n_e \chi_e (P) \nabla_\rho T_e$, and (d) $q_e = q_0 (P) - n_e \chi_e \nabla_\rho T_e$. P is a proxy for a heat flux dependency on the time scale of $p(\rho, t)$. Projections (b)-(d) are only valid for symmetric block-wave modulation forms.

experimental conditions are summarized. The Large Helical Device (LHD) [12] is a heliotron-type machine which is free from macroscopic magneto-hydrodynamic instabilities that could distort transport studies. LHD has a major radius of 3.5≈3.9 m and a typical effective (averaged) minor radius a_{99}≈0.6 m. The dimensionless radius ρ is defined here as r_{eff}/a_{99}. This is similar to the dimensionless radius ρ in tokamaks. The magnetic field strength at the magnetic axis 3.6 m is 2.75 T. Thomson scattering measurements are used to obtain the density profiles. The averaged static density at $\rho = 0$ is 3.6 10^{19} m^{-3} which smoothly decays to 3.44 10^{19} m^{-3} at $\rho = 0.47$. The entire density profile is shown in [6, Fig. 2a]. The corresponding time evolution of the density profile is measured using a 13-channel far-infrared interferometer (FIR), which measures the line-averaged densities [13]. These line-averaged densities are fluctuating less than 1% [6, Fig. 3b] when averaged over periods (the relevant frequency range). Hence, the density profile is considered in steady-state.

Steady-state balanced neutral beam injection of 2 MW is used in this discharge. In addition, modulated electron cyclotron heating is used with a duty cycle of approximately 50% with a period of 0.04 s (25 Hz). The corresponding frequency of the gyrotron is 77 GHz. Consequently, the main component of the deposition is at $\rho \approx 0.2$. The electron temperature was measured using electron cyclotron emission (ECE) by a 28-channel radiometer [14] and calibrated using a Thomson scattering system [15]. It is important to note that the electron-ion energy exchange time is approximately 0.6 s [6], which is significantly longer than the modulation period of 0.04 s. A more detailed description of this discharge can be found in [6].

3.2. Ideal frequency domain filtering and conditional average

Calculating the heat flux over the full time trace of a discharge is generally not feasible due to the noise level being too high. Hence, to reduce the noise level, periodic measurements are used allowing to average out the noise and to study the dynamic behavior. In [6] a method called conditional averaging is used. Conditional averaging refers generally to a more advanced method applying statistics on various samples and selecting data based on their statistics [16]. However, conditional averaging in [6] refers to a simple average over periods in the time domain. In other words, the data is separated in blocks of time data corresponding to a full period of the applied perturbation. These windows are averaged over the blocks. Moreover, a low-pass filter is applied in [6] to reduce the high frequent noise level necessary to calculate the derivative. The latter also means that the high frequent components related to the perturbation, i.e., heat flux physics, are suppressed and become biased. This can be seen in Fig. 3(a) where a moving average filter with length 2 ms is used. The advantage of using a moving average filter is that it has unit group delay and hence the phase (time delay) is not distorted. On the other hand, filters with a stronger cut-off often distort also the phase characteristic which is undesired. Note that taking conditional average or taking the fast Fourier transform (FFT) over the entire time trace are mathematically equivalent.

This work will take a different approach by removing all noise not related to the perturbation, which leads to a signal-to-noise ratio increase of a factor $\approx$ 100 dB ($6 \cdot 10^6$) compared to the unfiltered original signal under the assumption of stationary noise. This may come as a surprise, but in reality this is exactly what we exploit in case of perturbative experiments. In such experiments only frequency lines

September 21, 2018
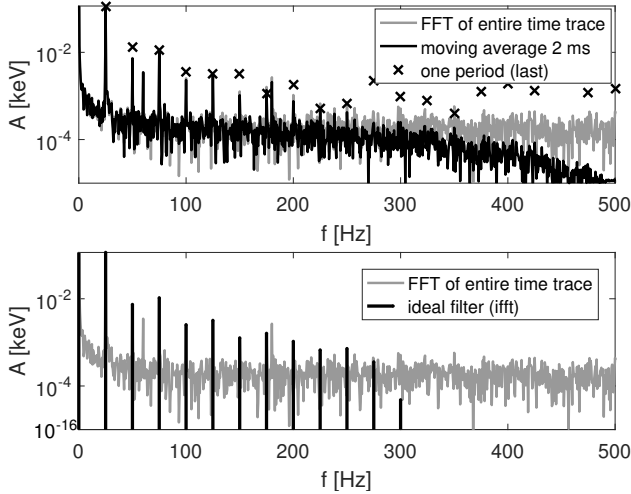
Figure 3. Comparison (a) moving average filter and (b) ideal filter. Note that 300 Hz has been suppressed due to electrical network disturbance (LHD#111121, $\rho = 0.47$). Moreover, the spectrum of the last period (one period) is shown to show the importance of using averaging either through the FFT or conditional averaging.

or harmonic components that are excited by the source (and possible higher and intermodulation harmonic components of the harmonic components of the source) are considered [4]. This is what we apply here as can be seen in Fig. 3(b). Possible variations over periods contribute to the stochastic uncertainties. Of course, it is still possible to remove certain periods from the signal, if they are subject to spurious plasma disturbances. Moreover, the phase will also remain unchanged.

The filtering in Fig. 3(b) is known as an ideal filter as it is non-causal and hence cannot be used to reduce the noise in real-time unlike the moving average filter shown in Fig. 3(a). However, the heat flux is calculated a posteriori for which this filter is optimal in a linear sense. The next step is to determine which multiples of the modulation frequency are retained and which are noise dominated and as such should be removed. This is especially important with the view of the temperature derivative calculations necessary to reconstruct the heat flux. Therefore, the best method is to select the harmonic components based on a statistical analysis of the signal-to-noise ratio's of the individual harmonic components.

3.3. Three different ways to estimate the stochastic uncertainty

There are various methodologies to calculate the SNR of the harmonic components or the SNR of the total signal. Here, we consider three approaches to evaluate the SNR of the harmonic components and total signal, which under the standard assumption of zero-mean

stationary white-noise are equivalent. The first step in the estimation of the heat flux common to all approaches is to calculate the variance of the stochastic uncertainties.

(i) Time domain: calculate variance over periods where the mean is equivalent to the conditional average. This gives the variance per time-sample. Under the assumption of zero-mean stationary white-noise, these can be averaged over time samples to find the variance of the entire time trace. Note that without the assumption of zero-mean stationary white-noise it becomes very difficult to calculate the variance of the ideally filtered temperature signals and the variance of the derivative. This method is abbreviated with *ca* (from conditional average).

(ii) Take Fourier transform per period and calculate the variances over the individual harmonic components. This gives the variance per frequency line. Under the assumption of zero-mean stationary white-noise, this variance should be equal within its statistical uncertainty for all frequency lines. As such this calculation simultaneously checks if the assumption of stationary white-noise is valid. The definitions can be found in [17]. This method is abbreviated with *caf* (from conditional average in the frequency domain).

(iii) Take Fourier transform over the entire time trace (can also be done per period) and uses the frequency lines surrounding the excited frequency lines to estimate the variances. This method is reliable if the surrounding frequencies are not influenced by the perturbation, transients, disturbances (e.g. 60 Hz), and the noise is locally constant around the excited frequency line [18]. As there are generally several surrounding frequency lines around an excited harmonic they can be averaged to attain a good variance estimate. Moreover, if the amplitude of the perturbation such as the electron cyclotron heating (ECH) fluctuates over periods this method is more reliable than the first two as it will not be added to the variance. This method is abbreviated with *sur* (from the surrounding frequency lines).

These methods are applied to the same time trace of the Large Helical Device as in [6]. However, with the important note that due to improved ray-trace algorithms for deposition and calibration [19], the results are slightly different. The spectrum of one ECE channel is shown in Fig. 4, including the standard deviations calculated based on the above methodologies. The calculated standard deviations are very similar (note the logarithmic scale). Only
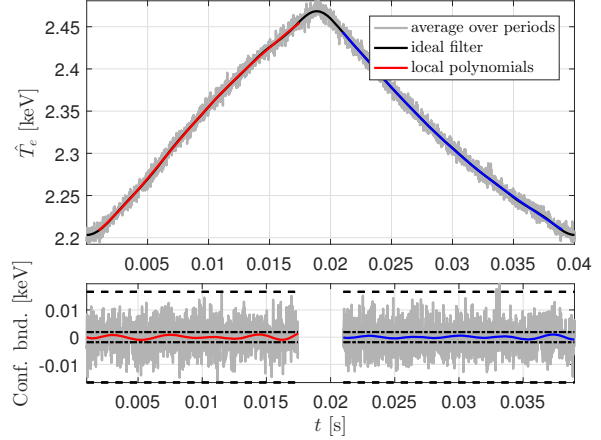
September 21, 2018
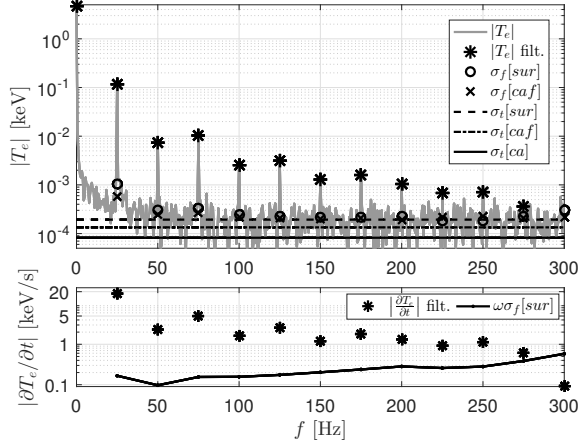
Figure 4. Spectrum of one time trace of LHD#111121 ($\rho = 0.47$). (a) Shows the noisy signal in grey, the filtered signal with stars. Moreover, the estimates of the standard deviation for the signal are shown, where σ_f is the standard deviation in the frequency domain and σ_t time domain (stationary white noise, i.e., flat spectrum). The abbreviations stand for *sur*: surrounding frequency lines used to calculate variance, *caf*: variance per frequency line, *ca*: variance calculated over over windowed time samples. (b) Amplitude of the time derivative of T_e calculated through the multiplication with $i\omega$ and the corresponding standard deviation of the individual frequency lines in the time derivative spectrum.

Figure 5. (a) LHD#111121 ($\rho = 0.47$) temperature signal after averaging over periods (conditional average without moving average filter). In black the signal based on ideal filtering and in color the piece-wise polynomial approximations. (b) Difference between piece-wise polynomial approximation and the averaged signal (grey) and in color the difference between the piece-wise polynomial approximation with the ideally filtered signal. Also the corresponding confidence bounds based on a Gaussian distributed noise with a 95% confidence interval are shown where the dashed-line is confidence bound for the averaged over periods time trace and the dashed-dotted line the ideally filtered signal. Note that the difference between the piece-wise polynomial approximation and the ideally filtered signal resides perfectly within the confidence bounds.

at low-frequency there is some deviation due to the transient, which could be further improved using the LPM-method introduced in [20, 21].

Methods number (II) or (III) are used to calculate the variance, i.e., the SNRs, of the individual harmonic components. Based on these SNRs harmonic components can be selected. As a rule of thumb, the minimum SNR of each harmonic component that should be considered is approximately 5 dB because Gaussian noise conditions are retained for SNR > 5 dB [17]. For the channel chosen here, this is 275 Hz (in Fig. 4, at 275 Hz, SNR is $\approx$ 4.7 dB). For channels closer to the source the frequency with a SNR> 5 dB is higher and further away from the source this is generally lower. We have decided to use for all the channels the same harmonic components, but this is up to the user. Even if many excited harmonics are selected for the ideally filtered signal, the variance drops significantly as the variances of the intermediate lines only related to noise and disturbances are removed. This is discussed and shown in detail in the next section.

3.4. Reconstructed temperature signals after filtering

After removing the harmonic components which are related to noise and other disturbances, e.g., 60 Hz electric network, the inverse Fourier transform is applied to reconstruct the temperature signal in the time domain. The corresponding noise variances can

be found in Fig. 4. For one time trace the filtered T_e signal can be seen in Fig. 5. The filtered T_e signal is compared to the signal averaged over periods and to a piece-wise polynomial approximation, which is discussed in the next section. The colour red corresponds to when the ECH is on and blue when the ECH is off.

In Fig. 5(b), the 95% confidence bounds ($1.96\sigma_t$) are plotted based on the additional assumption of Gaussian distributed noise. The difference in confidence bounds between the ideally filtered signal and original signal again confirms the significant reduction in noise level. Moreover, the confidence bounds properly include the measurement data (dashed lines) and the filtered approximation (dash-dotted lines).

In the next section is discussed how to calculate the derivatives from the filtered temperature signals necessary to reconstruct the heat flux.

4. Derivative calculation

The calculation of the temperature derivatives in time and space are the key problems in estimating the heat flux directly. There is not a clear answer to what methodology should be used as the smoothness of the derivative depends on how the high-frequencies
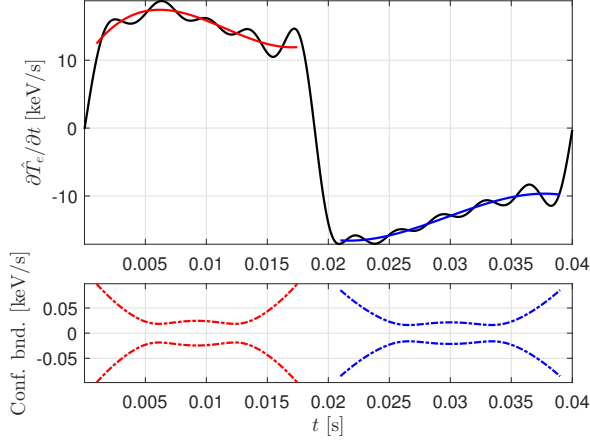
Figure 6. (a) Time derivative of the ideally filtered signal (black) and the polynomial approximation (color). (b) The corresponding confidence bounds propagated from the measurements to the polynomial fit. Note its time-dependent behavior (LHD#111121, $\rho = 0.47$).

of the temperature spectra are cut-off. This cut-off is necessary, as in the frequency domain taking the derivative is equivalent to multiplying the harmonic components by $i\omega$ and as such at high-frequencies noise is amplified significantly. Specifically, for the block wave modulation there is an additional issue. The temperature changes its direction when turning on and off of the power source (in Fig. 5 at 0 and 0.02 s). Under standard transport assumptions, the temporal temperature derivative is discontinuous at this point in time. As such it is senseless to calculate or interpret the derivative at this sign change of the temperature derivative. These are the reasons for introducing a second methodology to calculate the derivative using a piece-wise polynomial reconstruction next to the harmonic reconstruction of the derivative based on the filtered temperature spectra.

4.1. Harmonic reconstruction

The harmonic reconstruction uses the harmonic components selected in the previous section and multiplies them with $i\omega$. Then, the inverse Fourier transform is applied to arrive at the time derivative of the temperature. This is shown by the black line in Fig. 6. The derivative contains large oscillations. These oscillations are largely the result of truncation of the Fourier coefficients of the T_e due to the filtering applied and as such are not related to the physics. This phenomenon is known as the Gibbs effect. Although the Gibbs effect is small in the temperature signal shown in Fig. 5, the oscillations are amplified in the derivative calculation leading to a devastating effect on the time derivative $\partial T_e / \partial t$. Moreover, due to the

truncation at the discontinuity of the temperature, the derivative is now smooth and as such is unreliable. Nevertheless, the overall shape of the derivative is reliable with the exception of the oscillations and smoothness at the sign changes. It is possible to increase the smoothness of the derivative by using additional low-pass filtering, which could be done in both frequency and time-domain. However, such changes would be aesthetic and would only lead to a change in the bias-variance relationship rather than the true derivative [22]. This also means that calculating the corresponding variance (standard deviations must be multiplied by $i\omega$) of the derivative based on the ideally filtered T_e calculation is also unreliable. Therefore, an alternative method which significantly suppresses the self-introduced Gibbs oscillations and allows for a calculation closer to the non-smooth sign change point is used. It is based on a piece-wise polynomial reconstruction, which also allows for a proper confidence analysis.

4.2. Piece-wise polynomial reconstruction

The removal of high frequent excited harmonic components is a necessity to arrive at a significant improvement of the SNRs. However, the associated self-introduced Gibbs oscillations need to be suppressed to arrive at a proper derivative estimate. As the input power is generally constant over a large time trace, it is reasonable to assume that also the temperature should increase steadily without oscillations. Hence, instead of calculating the derivative directly, the temperature is approximated by a polynomial for the part of the time trace associated with a constant power. Thereby, simultaneously avoiding the problem of the derivative calculation at the sign change of the derivative. Here, we use a standard polynomial of order n

$$\hat{T}_e(t) = \theta_1 t^n + \theta_2 t^{n-1} + \ldots + \theta_n t + \theta_{n+1}. \quad (6)$$

This polynomial can be estimated using a simple least squares fit

$$T_e = H\theta + V, \quad (7)$$

where the measurement noise on the time traces is included via V, which is characterized by the covariance matrix using the assumption of non-zero stationary white-noise $C_V = \sigma_t^2 I$ (I, identity matrix). The standard deviation σ_t is shown in Fig. 4. The matrix H is known as the Vandermonde matrix. The least-squares solution is given by

$$\theta = \left(H^T C_V^{-1} H\right)^{-1} H^T C_V^{-1} y, \quad (8)$$

with its corresponding covariance matrix

$$C_\theta = \left(H^T C_V^{-1} H\right)^{-1}. \quad (9)$$

September 21, 2018

This relationship is rather simple due to C_V being the identity matrix times σ_t^2. This procedure is repeated for every interval where the power level is constant. A fourth order piece-wise polynomial reconstruction of T_e is shown in Fig. 5(a). The differences between the harmonic reconstruction in black and the piece-wise polynomial reconstruction are within the statistical confidence of the measurements (see Fig. 5(b)). Alternatively, the order of the polynomial can be selected automatically by calculating the minimum of the residue for various orders of the polynomial fit. Of course it is possible to use other approximations for the time evolution such as least-square spline approximations [23]. We have chosen for the polynomial approximation for its ease in calculating corresponding variances and time derivatives.

Then, the time derivative van be calculated by reducing the order of the polynomial, i.e.,

$$\frac{\partial \hat{T}_e}{\partial t} = n\theta_1 t^{n-1} + (n-1)\theta_2 t^{n-2} + \ldots + \theta_n. \quad (10)$$

The corresponding variance is given by

$$\sigma_{\partial t}^2(t) = J_{\partial t}(t) C_\theta J_{\partial t}(t), \quad (11)$$

where $J_{\partial t} = \left[n\,t^{n-1}, (n-1)\,t^{n-2}, \ldots, 1, 0\right]$. Note that this also means that the variance becomes time dependent, which is a logical consequence of taking the derivative ($i\omega$-multiplication in the frequency domain). The resulting time derivative can be seen in Fig. 6. It does not have the problem of the oscillations and follows approximately the center of the derivatives calculated using the harmonic reconstruction. Moreover, the derivative can be approximated in a large range.

The variances are based on the propagation of uncertainty of the measurements to the polynomial and then to its derivative as such they are not subject to the oscillations. Hence, the confidence bounds are much smaller than the difference between the ideal filtered signal and the polynomial fit. The confidence bounds are exact under the assumption that the piece-wise polynomial is the correct description of the physics due to a change in heating power. If this assumption is not fulfilled a so-called bias-variance relationship holds again, see for details [22]. It is also important to note that if the piece-wise polynomial fit is used, it is less relevant up till which excited frequency is truncated in the ideal filter, which was discussed in Sec. 3.4. The reason is that the higher harmonic components have only a small contribution to T_e. The intermediate (non-excited) frequency lines still need to be removed, of course.

Both derivatives will be used to calculate the heat flux, but the polynomial fit will also be used to calculate the variance on the heat flux.
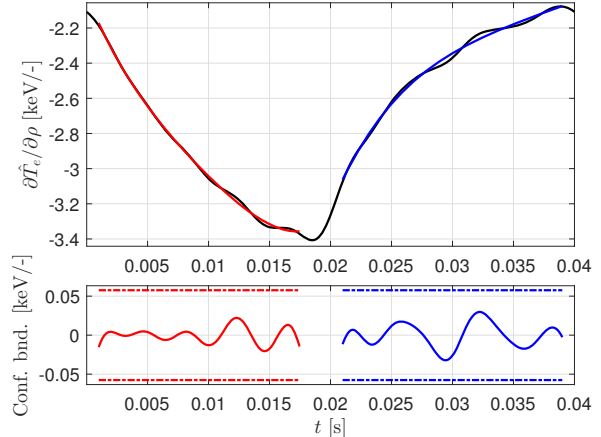
Figure 7. (a) Spatial derivative of the temperature signal of LHD#111121, around $\rho = 0.47$ of the ideally filtered signal (black) and the polynomial approximation (color). (b) Corresponding difference between ideally filtered signal and the polynomial approximation and the $1.96\sigma_{\partial\rho}$ confidence bounds on the polynomial approximation.

4.3. Spatial derivative

The spatial derivative is not necessary for the calculation of the heat flux. However, we also want to determine the effective diffusion coefficient from the projection in $q_e - \nabla_\rho T$ plane. Therefore, the spatial temperature derivative also needs to be determined. As we want to estimate the local gradient, we have decided to use a local approximation instead of a spatial derivative of a spline or polynomial approximation of the radial profile. Moreover, we want to retain the symmetry of the derivative, hence, a central difference is used to approximate the derivative

$$\frac{\partial \hat{T}_e}{\partial \rho}(\rho_n, t) \approx \frac{T_e(\rho_{n+1}, t) - T_e(\rho_{n-1}, t)}{\rho_{n+1} - \rho_{n-1}}. \quad (12)$$

On the boundaries and in the case that measurement channels are too far apart, a one-sided finite difference approximation is used. One can debate which $\hat{T}_e$ should be used. We have chosen to use the polynomial fit to suppress the oscillations (Gibbs effect). However, as the spatial derivative is less subject to the oscillations, one could also use the ideally filtered temperature $\hat{T}_e$. The variance of the spatial derivative is approximated using propagation of uncertainty, i.e.,

$$\sigma_{\partial\rho}^2(\rho_n) \approx (\rho_{n+1} - \rho_{n-1})^{-2} \left(\sigma_t^2(\rho_{n+1}) + \sigma_t^2(\rho_{n-1})\right). \quad (13)$$

Fig. 7 shows both the resulting approximation methodologies for the spatial derivative. Moreover, it shows that due to the piece-wise polynomial approximation there is again suppression of the

September 21, 2018

oscillations, but with respect to the variance the effect is small.

5. Reconstructed heat flux and effective diffusion estimate

In this section, the heat flux is calculated including its variance. Moreover, it is shown how to calculate the effective diffusion coefficient.

5.1. Estimating heat flux

It is rather straightforward to calculate the heat flux as it only requires taking the spatial integral and the inclusion of the density, power modulation and deposition profile. Therefore, this section briefly discusses how the integral is taken and how the resulting variance on the heat flux is calculated. First, the time derivative of the stored power is calculated with

$$\frac{\partial \hat{W}}{\partial t} = n(\rho, t) \frac{\partial \hat{T}_e}{\partial t}. \tag{14}$$

The heat flux is defined by the integral

$$q_e(\rho, t) = \frac{1}{\rho} \int_0^\rho \rho Q(\rho, t) \, d\rho, \tag{15}$$

where

$$Q(\rho, t) = \frac{\partial \hat{W}}{\partial t} - p(\rho, t). \tag{16}$$

The heat flux is then calculated by approximating the integral in (15) using the trapezoidal rule

$$q_e(\rho_n, t) \approx \frac{1}{2} \frac{1}{\rho_n} \sum_{n=1}^N (\rho_{n+1} - \rho_n)$$
$$[\rho_n Q(\rho_n, t) + \rho_{n+1} Q(\rho_{n+1}, t)]. \tag{17}$$

The resulting calculated heat flux is shown in Fig. 8(a) as function of time and Fig. 8(c) as function of the spatial gradient. As the oscillations are averaged due to the integration of space the difference between the polynomial reconstruction and harmonic reconstruction are comparable with respect to the confidence bounds. Except at the end points of the polynomial reconstructions close to the sign-change of the derivatives, which is logical as the harmonic reconstructions are unreliable due to the smoothed discontinuous derivative of $\hat{T}_e$. Also the phase difference between the source and the temperature signal can have impact on this reconstruction.

We also see that the heat flux loop is not closed (in comparison to Fig. 1), which has two possible reasons: 1) an error in the deposition profile calculation [24] and 2) non-local transport on the time-scale of the heating power modulation [5]. It can be shown that both explanations are mathematically equivalent, but are of course very different in terms of the physics. Although this methodology allows further investigation of this important physics problem, it is not the subject of this paper. Hence, we will not further analyze it here.

Additionally, errors in how $p(\rho, t)$ is filtered or treated contributes to errors at the transition of the levels. We have chosen to filter $p(\rho, t)$ exactly as we have filtered T_e, i.e., using the same harmonic components. The reason is that as (16) is a power balance and filtering is equivalent to removing energy from the measurements, the energy balance is best preserved. However, as $p(\rho, t)$ is discontinuous at the power steps truncation of the Fourier coefficients results in a much more significant Gibbs oscillations (see Fig. 8(c)). Alternatively, one can use simply the signal itself or all the higher harmonics, but this causes strange discontinuities at the change of heat flux levels. Therefore, there is no clear choice for filtering for $p(\rho, t)$, but for both hold that they are reliable in the main region of the piece-wise polynomial reconstruction.

5.2. Variance calculation on heat flux

The stochastic confidence on the calculations can also be assessed as is explained in this section. Both the density $n_e(\rho, t)$ and heating powers $p(\rho, t)$ variances can be evaluated equivalently as is explained for $\hat{T}_e$. Then, the variance of the density $\sigma_{n_e}^2(t)$ and $\sigma_{\partial t}^2(t)$ need to be combined. As the density $n_e(\rho, t)$ can be considered independent of $\hat{T}_e$ this results in

$$\sigma_{\partial W}^2(t) = \left(\frac{\partial \hat{W}}{\partial t}\right)^2 \left(\left(\frac{\sigma_{n_e}(t)}{n(t)}\right)^2 + \left(\frac{\sigma_{\partial t}(t)}{\partial \hat{T}_e/\partial t}\right)^2\right). \tag{18}$$

In this discharge the density time fluctuations are neglible in the relevant frequency range, hence, $\sigma_{n_e}(t) = 0$. Static calibration errors could also be included using $\sigma_{n_e}^2(t)$ and $\sigma_{\partial t}^2(t)$. Then, the calibration error needs to be translated to variances, which in the Gaussian case can be done using confidence intervals for the translation of calibration errors into variances. Calibration errors do not affect the time evolution when the perturbations are small. Including extra variance using calibration errors would result in a larger confidence interval of the diffusion coefficient. In absolute sense this would be correct, however, it would suggest that the relative difference in diffusion coefficients as function of time is less significant, which would be an incorrect assessment. Hence, we have decided not to include these static calibration errors, but focus on the perturbative uncertainties. Then, the variances for $\partial \hat{W}/\partial t$ and

September 21, 2018
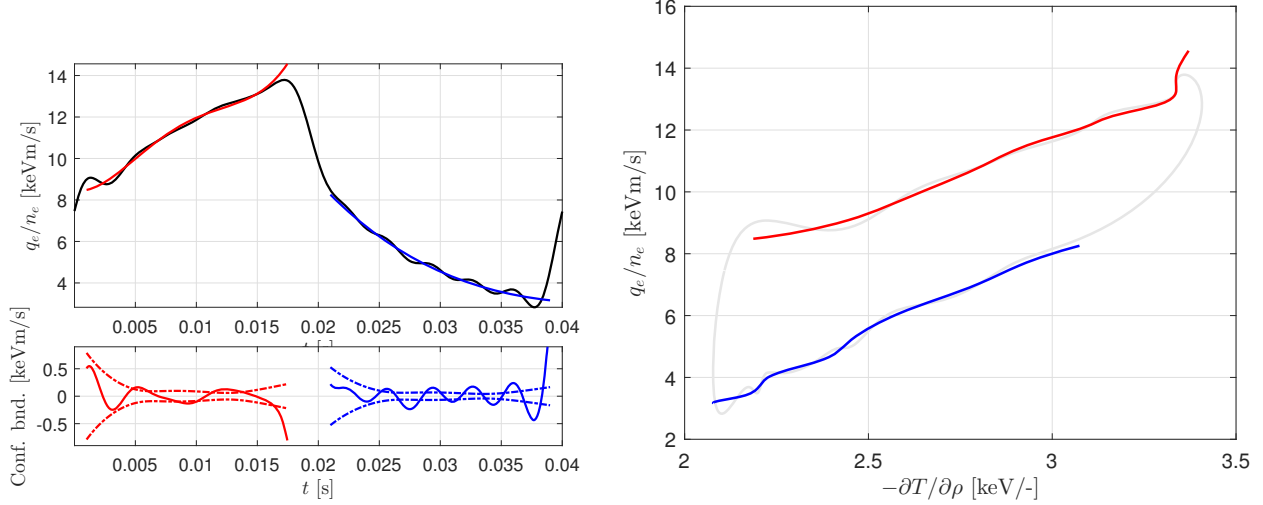
Figure 8. (a) Time evolution of the normalized heat flux using the ideally filtered signal (black) and the polynomial approximation (color) (LHD#111121, around $\rho = 0.47$). (b) Difference between ideally filtered signal and the polynomial approximation and $1.96\sigma_q(t)$ confidence bounds on the polynomial approximation. (c) Normalized heat flux versus $-\partial T/\partial\rho$ for both the approximations.

$p(\rho, t)$ need to be combined, which originate from independent measurements such that

$$\sigma_Q^2(t) = \left(\frac{\partial \hat{W}}{\partial t}\right)^2 \sigma_{\partial W}^2(t) + p(\rho, t)^2 \sigma_p^2. \qquad (19)$$

Then, the variance of the integral based on propagation of uncertainty and averaging of noise (factor 2) is calculated as follows

$$\sigma_q^2(\rho, t) \approx \rho_n^{-2} \sum_{n=1}^{N} \frac{(\rho_{n+1} - \rho_n)^2}{2}$$
$$\left[\rho_n^2 \sigma_{\partial q}^2(\rho_n, t) + \rho_{n+1}^2 \sigma_{\partial q}^2(\rho_{n+1}, t)\right]. \quad (20)$$

Given that at small ρ only a few samples are available, it is important to remember that there is an additional error on the estimate based on the formula for the trapezoidal approximation, i.e.,

$$\varepsilon_q(\rho_n) = -\frac{(\rho_n)^2}{12N^2}\left[\frac{\partial Q}{\partial \rho}(\rho_n) - \frac{\partial Q}{\partial \rho}(0)\right] + \mathcal{O}(N^{-3})$$
$$(21)$$

which converges rapidly to zero. Also it is important to note that errors in measurements at small radii or uncertainty in the radii propagates in the estimate of q_e, hence, in reality the errors on the estimate can be larger. However, as the we do not know the derivative of $Q(\rho, t)$ or deterministic errors in radii and the other measurements. Therefore, we will not further consider these errors in (21), but focus purely on the stochastic uncertainties. The 95% confidence bounds based on (20) assuming Gaussian distributed noise is shown in Fig. 8.

5.3. Effective diffusion calculation from projection

One of the applications of plotting the perturbative heat flux is the determination of the effective diffusion coefficient. The effective diffusion coefficient is generally defined as the tangent to the heat flux in the $q_e - \nabla_\rho T_e$ plane [4]. If the deposition profile is calculated correctly and there are no non-local contributions and the transport is purely diffusive, independently from the source modulation form, the diffusion coefficient can be calculated from this tangent (see Fig. 1). However, one or more of these conditions are generally not valid in practice. Therefore, the Lissajous-like curve opens up as can be seen in Fig. 8. How it opens up depends specifically on what kind of power modulation wave form is used for $p(\rho, t)$ in the heat flux definition in (4). Consequently, the tangent is not necessarily a proper definition of the effective diffusion coefficient. Therefore, the method presented here should only be used in case of a block-wave modulation with constant power levels to determine the effective diffusion coefficient, which is one of the most common modulation scenario in laboratory fusion plasmas.

Fig. 8(c) is calculated using the measured time evolution of $p(\rho, t)$ for which the power density is shown in Fig. 9 for a few radial locations. In Fig. 5(a) and subsequent figures, it can be seen that the electron temperature changes direction at 0.016 ms. However, in Fig. 9 it changes at 0.02 ms. This is of course non-causal and originates from a synchronization error, which in principle can be compensated [6]. However, as shown in Fig. 8 it only has a significant impact on a small time interval of the heat flux reconstruction. Moreover, in Fig. 9 it can be seen that also the power

September 21, 2018
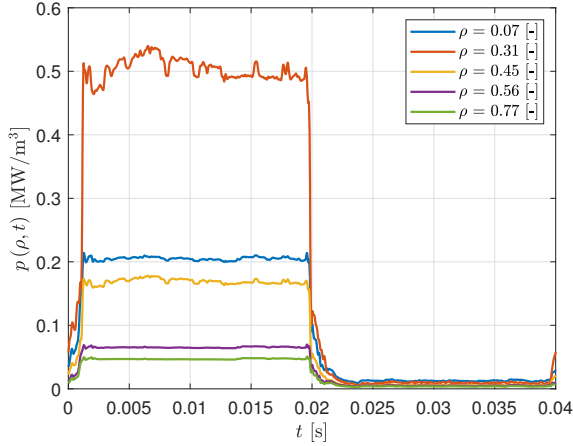
Figure 9. (a) Measured time evolution of the power deposition profile $p(\rho, t)$ (color) (LHD#111121)

density has a slow decay from 0.02 s to 0.025 s and has fluctuations in the measurements. It is questionable if these are actual changes or errors in the way $p(\rho, t)$ is measured and calculated. These possibly non-physical contributions are the reason for the non-straightness in Fig. 8(c) of the polynomials. However, it is not necessary to know or use the exact heat deposition density profile to calculate the diffusion coefficients. It is sufficient to know that constant power levels for $p(\rho, t)$ have been used. This can be shown by analyzing the 50% duty-cycle in detail. For the 50% duty-cycle the time evolution of $p(\rho, t)$ is defined as follows

$$p(\rho, t) = \begin{cases} p_1 & 0 < t \leqslant \frac{c}{2} & \text{ECH-on} \\ p_2 & \frac{c}{2} < t \leqslant c & \text{ECH-off} \end{cases}, \qquad (22)$$

where c is one period [s]. Consequently, the heat-flux can be separated into two parts

$$q_e(\rho, t) = \begin{cases} \frac{1}{\rho} \int_0^\rho \rho \frac{\partial \hat{W}}{\partial t} d\rho + Q_1 & 0 < t \leqslant \frac{c}{2} & \text{ECH-on} \\ \frac{1}{\rho} \int_0^\rho \rho \frac{\partial \hat{W}}{\partial t} d\rho + Q_2 & \frac{c}{2} < t \leqslant c & \text{ECH-off} \end{cases},$$
$$(23)$$

with constant levels as was the case in Fig. 8. As the constants Q_1 and Q_2 do not contribute to the slope (effective diffusion coefficients), they can be ignored for the slow-time scale. Therefore, it suffices to calculate the integral

$$q_{\partial T/\partial t}(\rho, t) = \frac{1}{\rho} \int_0^\rho \rho \frac{\partial \hat{W}}{\partial t} d\rho, \qquad (24)$$

avoiding the introduction of an extra uncertainty component on $p(\rho, t)$ into the estimate of χ_e^{eff}. Its corresponding variance is given by

$$\sigma_{q_{\partial T/\partial t}}^2(\rho, t) \approx \rho_n^{-2} \sum_{n=1}^N \frac{(\rho_{n+1} - \rho_n)^2}{2}$$
$$\left[\rho_n^2 \sigma_{\partial W}^2(\rho_n, t) + \rho_{n+1}^2 \sigma_{\partial W}^2(\rho_{n+1}, t) \right]. \quad (25)$$

Fig. 10 shows the temperature dependent part of the heat flux calculated with (24) for the analyzed discharge. The constant levels are different from Fig. 8(c) due to the omission of $p(\rho, t)$. Moreover, due to this omission the slopes are no longer subject to the Gibbs effect and even though a fourth order piece-wise polynomial approximation is used the slopes are remarkably constant. Hence, a large part of the slope for a respective power level is used to estimate the effective diffusion coefficient.

Both $\partial T(t)/\partial \rho$ and $q_{\partial T/\partial t}(t)$ are uncertain quantities with time-varying variances. Therefore, the effective diffusion estimation problem is an errors-in-variables problem and needs to be solved using a maximum likelihood estimation. However, if we compare the noise levels of $\partial T(t)/\partial \rho$ and $q_{\partial T/\partial t}(t)$ with respect to the change of the signal, we note that the variance on $\partial T(t)/\partial \rho$ is rather small compared to that of $q_{\partial T/\partial t}(t)$. Hence, to simplify the calculation the variance on $\partial T(t)/\partial \rho$ is ignored. As such the estimation problem for χ_{eff} can be calculated based on (8) and its covariance (9) (with $n = 1$ in (6)). Of course, the absolute levels of the heat flux have no physical meaning as Q_1 and Q_2 in (23) have been omitted, which is attested by the negative heat-flux.

The resulting estimate of χ_{eff} with 1.96σ bounds are given in Fig. 10 on the spatial derivative and heat flux. The resulting estimate of the effective diffusion coefficient with ECH on (red) is $\chi_{eff} = 4.71 \pm 0.01$ m^2/s and off (blue) is $\chi_{eff} = 5.41 \pm 0.01$ m^2/s. The small confidence bounds are a consequence of the slopes being remarkably straight, this also suggests that other effects such as convective velocity and damping are negligible compared to the diffusion component of transport. Note that fast transport components and errors in the deposition profile cannot be seen here as they contribute to the difference in power levels and not in the slopes. On the other hand, the power dependence of the diffusion coefficient can be studied due to the separation of slopes for the corresponding power levels as is discussed in, e.g., [25, 26]. The corresponding effective diffusion coefficient in steady-state is given by the diffusion coefficient that has been estimated using the slope for the corresponding power level. Note that the power balance diffusion coefficient is not determined by the slopes, but depends implicitly on the total heat flux.

6. Conclusion

This paper shows that by applying physics based filtering and assumptions, that the heat flux can be reconstructed with high accuracy. Consequently, the physics structure of the heat flux can be studied in more detail. Moreover, a full variance

September 21, 2018
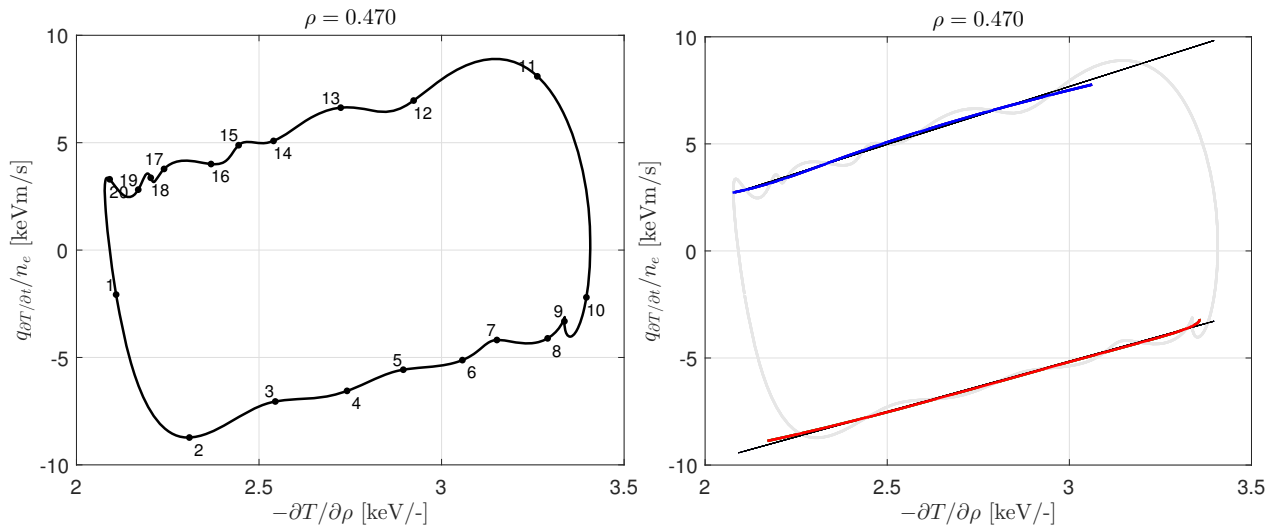
Figure 10. (a) Normalized heat flux based on temperature only versus $-\partial T/\partial \rho$ based on harmonic reconstruction where the · represents increments of $\Delta t = 2$ ms. (b) Normalized heat flux based on temperature only versus $-\partial T/\partial \rho$ based on polynomial approximation. (LHD#111121, around $\rho = 0.47$)

analysis is performed such that the confidence of the reconstructed heat flux can be assessed.

The two major improvements in the heat flux calculations are based on exploiting the property that only the excited harmonic components are relevant in the temperature measurements and that the heating power is constant over a large time interval such that the change in temperature over time is smooth and not oscillating. These two properties have been exploited through the use of an ideal filter and the piecewise polynomial approximation thereby significantly increasing SNRs and stabilizing the calculation of the time derivative of the temperature. Moreover, these processes are statistically well defined such that a confidence analysis can be performed. The method is applied to measurements from the Large Helical Device thereby showing the merit of this methodology. Moreover, as the heat flux estimates at LHD show that at the slow time-scale transport can be considered diffusive (straight lines), it is also possible to estimate the (effective) diffusion coefficient. In the future, this estimation will be a valuable tool in the experimental analysis of power dependent diffusion coefficients as suggested in [5], in the estimation of power deposition profiles in relation to missing power [24], and critical gradient type heat -flux dependencies next to convective velocities, damping, and the effect of boundary conditions.

Acknowledgments

References

[1] Ryter F, Angioni C, Beurskens M, Cirant S, Hoang G T, Hogeweij G M D *et al.* 2001 *Plasma Phys. Control. Fusion* **43** A323 URL http://stacks.iop.org/0741-3335/43/i=12A/a=325

[2] Ryter F, Dux R, Mantica P and Tala T 2010 *Plasma Phys. Control. Fusion* **52** 124043

[3] Mantica P and Ryter F 2006 *C. R. Phys.* **7** 634–649

[4] Lopes Cardozo N J 1995 *Plasma Phys. Control. Fusion* **37** 799

[5] Stroth U, Giannone L, Hartfuss H J, ECH Group and the W7-AS Team 1996 *Plasma Phys. Control. Fusion* **38** 611

[6] Inagaki S, Tokuzawa T, Tamura N, Itoh S I, Kobayashi T, Ida K, Shimozuma T, Kubo S, Tanaka K, Ido T *et al.* 2013 *Nucl. Fusion* **53** 113006

[7] Jacchia A, Mantica P, De Luca F and Gorini G 1991 *Phys. Fluids B-Plasma* **3** 3033–3040

[8] van Berkel M, Zwart H J, Tamura N, Hogeweij G M D, Inagaki S, de Baar M R and Ida K 2014 *Phys. Plasmas* **21** 112507

[9] Garbet X, Sarazin Y, Imbeaux F, Ghendrih P, Bourdelle C, Gürcan ï D and Diamond ï D 2007 *Phys. Plasmas* **14** 122305

[10] Mantica P, Gorini G, Hogeweij G M D, Lopes Cardozo N J and Schilham A M R 2000 *Phys. Rev. Lett.* **85**(21) 4534–4537

[11] van Berkel M *et al.* 2018 *under revision in nucl. fusion*

[12] Iiyoshi A, Komori A, Ejiri A, Emoto M, Funaba H, Goto

M, Ida K, Idei H, Inagaki S, Kado S *et al.* 1999 *Nucl. Fusion* **39** 1245

[13] Tanaka K, Michael C, Sanin A, Vyacheslavov L, Kawahata K, Murakami S, Wakasa A, Okajima S, Yamada H, Shoji M *et al.* 2006 *Nuclear fusion* **46** 110

[14] Kawahata K, Nagayama Y, Inagaki S and Ito Y 2003 *Rev. Sci. Instrum.* **74** 1449–1452

[15] Yamada I, Narihara K, Funaba H, Minami T, Hayashi H, Kohmoto T, Group L E *et al.* 2010 *Fusion Sci. Technol.* **58** 345–351

[16] Billingsley P 2012 *Probability and measure* (John Wiley and Sons, Hoboken (NJ))

[17] van Berkel M, Zwart H J, Hogeweij G M D, Vandersteen G, van den Brand H, de Baar M R and the ASDEX Upgrade Team 2014 *Plasma Phys. Control. Fusion* **56** 105004.

[18] Pintelon R and Schoukens J 2012 *System Identification: A Frequency Domain Approach* (John Wiley and Sons, Hoboken (NJ))

[19] Ii T, Kubo S, Takahashi H, Makino R, Seki R, Yoshimura Y, Igami H, Shimozuma T *et al.* 2015 *Nucl. Fusion* **55** 123019 URL `http://stacks.iop.org/0029-5515/55/i=12/a=123019`

[20] van Berkel M, Kobayashi T, Igami H, Vandersteen G, Hogeweij G M D, Tanaka K, Tamura N, de Baar M R, Zwart H J, Kubo S, Ito S, Tsuchiya H and the LHD Experiment Group 2017 **57**

[21] Pintelon R, Schoukens J, Vandersteen G and Barbé K 2010 *Mech. Syst. Signal Pr.* **24** 573–595

[22] Hall B 2010 *Nonparametric Estimation of Derivatives with Applications* Doctoral dissertations, Paper 114 University of Kentucky URL `http://uknowledge.uky.edu/gradschool_diss/114`

[23] de Boor C 2001 *A Practical Guide to Splines* (Springer-Verlag, Berlin-Heidelberg)

[24] Romé M, Erckmann V, Gasparino U, Hartfuss H J, Kühner G, Maaï¿œberg H and Marushchenko N 1997 *Plasma Phys. Control. Fusion* **39** 117

[25] Hartfuss H J, Endler M, Erckmann V, Gasparino U, Giannone L *et al.* 1994 *Plasma Phys. Control. Fusion* **36** B17

[26] van Berkel M, Zwart H, Hogeweij G and de Baar M 2017 *Plasma Phys. Control. Fusion* **59** 062001

September 21, 2018